SUPPLEMENTARY INFORMATION

Mechanosensitive subcellular rheostasis drives emergent single-cell mechanical homeostasis

Shinuo Weng[a,#], Yue Shao[a,#], Weiqiang Chen[a,$], and Jianping Fu[a,b,c,*]

[a]Department of Mechanical Engineering, University of Michigan, Ann Arbor, MI 48109, USA;

[b]Department of Biomedical Engineering, University of Michigan, Ann Arbor, MI 48109, USA;

[c]Department of Cell and Developmental Biology, University of Michigan Medical School, Ann Arbor, MI 48109, USA.

[#]These authors contributed equally to this work; [$]Current address: Department of Mechanical and Aerospace Engineering, New York University, New York, NY 10012, USA;

*Correspondence should be addressed to J.F. (jpfu@umich.edu).

Supplementary Information:

SUPPLEMENTARY METHODS

Biophysical modeling

The biophysical model characterizing the dynamics of subcellular CSK tension and FA upon cell stretch was comprised of three key mechanisms: (1) integrin catch-slip bond[1], which was shown in this work as required for FA rheostasis (**Fig. 2l**); (2) F-actin catch-slip bond[2], to recapitulate catch-slip-like behaviors in the FA-CSK mechanical network; and (3) myosin motor activity[3], which drives muscle-like spontaneous contraction in response to external forces and was shown as required for FA rheostasis (**Fig. 2h**).

Integrin catch-slip bond

Force dependent association and dissociation of FA molecules were analyzed using a model described previously ('*Novikova-Storm* model'[4]) featuring a catch-slip bond between integrin $\alpha_5\beta_1$ and fibronectin $FNIII_{7\text{-}10}$[1]. Temporal evolution of FA size was thus expressed as

$$\frac{dN_{FA}}{dt} = k_{FA,on}\left(N_{FA}^{tot} - N_{FA}\right) - k_{FA,off} \cdot N_{FA} \quad (1)$$

, where N_{FA} represented the total number of integrin molecules contained in FA, N_{FA}^{tot} denoted the total number of integrin molecules available in the neighboring cytosol, and $k_{FA,on}$ and $k_{FA,off}$ were the association and dissociation rates of a single integrin catch-slip bond, respectively. For simplicity, $k_{FA,on}$ was assumed independent of force and was calculated as

$$k_{FA,on} = k_{FA,o} \cdot \gamma_{FA} \quad (2)$$

, where γ_{FA} was a dimensionless rate constant and $k_{FA,o}$ was a reference rate. $k_{FA,off}$ was characterized by a force-dependent function using a two-pathway model[5]

$$k_{FA,off} = k_{FA,o}\left[\exp\left(\frac{f}{f_{FA}^{*}} - \phi_{FA,s}\right) + \exp\left(-\frac{f}{f_{FA}^{*}} + \phi_{FA,c}\right)\right] \quad (3)$$

, where f denoted the force acting on a single integrin molecule, f_{FA}^{*} was a reference force for normalization, and $\phi_{FA,c}$ and $\phi_{FA,s}$ represented zero-force dissociation rates associated with the catch and slip portions of integrin catch-slip bond dynamics, respectively. Assuming that the total force exerted on FA F_{tot} was uniformly distributed on each single integrin molecule, an ordinary differential equation governing the dynamic evolution of FA size N_{FA} was obtained as

$$\frac{dN_{FA}}{d} = \frac{k_{FA,o}}{t}\left\{\gamma_{FA}\left(N_{FA}^{tot} - N_{FA}\right) - N_{FA}\left[\exp\left(\frac{F_{tot}}{f_{FA}^{*}\cdot N_{FA}} - \phi_{FA,s}\right) + \exp\left(-\frac{F_{tot}}{f_{FA}^{*}\cdot N_{FA}} + \phi_{FA,c}\right)\right]\right\} \quad (4)$$

Catch-slip bond of F-actin

Force-dependent association and dissociation of G-actin with F-actin have been demonstrated to follow a catch-slip bond model[2]. The association and dissociation rates of G-actin with F-actin $k_{ACT,on}$ and $k_{ACT,off}$ were thus written as

$$k_{ACT,on} = k_{ACT,o}\cdot\gamma_{ACT} \quad (5)$$

$$k_{ACT,off} = k_{ACT,o}\left[\exp\left(\frac{f}{f_{ACT}^{*}} - \phi_{ACT,s}\right) + \exp\left(-\frac{f}{f_{ACT}^{*}} + \phi_{ACT,c}\right)\right] \quad (6)$$

, where γ_{ACT} was a dimensionless rate constant, $k_{ACT,o}$ was a reference rate, f denoted force acting on F-actin, f_{ACT}^{*} was a reference force for normalization, and $\phi_{ACT,c}$ and $\phi_{ACT,s}$ represented zero-force dissociation rates associated with the catch and slip portions of F-actin catch-slip bond, respectively.

Given force balance and force transmission across the mechanical linkage between the actin CSK and FA, the total force acting on actin stress fibers was also denoted as F_{tot}. Actin stress fibers were modeled as bundled F-actin filaments with each filament comprising actin monomers connected in series. Assuming a uniform force distribution in stress fibers and that each F-actin filament in stress fibers was connected to one integrin molecule in FA, the force acting on each actin monomer along a F-actin filament was obtained as F_{tot}/N_{FA}. The ordinary differential equation governing dynamic evolution of the total number of actin monomers N_{ACT} in actin stress fibers was thus written as

$$\frac{dN_{ACT}}{d}=\frac{k_{ACT,o}}{t}\left\{\gamma_{ACT}\left(N_{ACT}^{tot}-N_{ACT}\right)-N_{ACT}\left[\exp\left(\frac{F_{tot}}{f_{ACT}^{*}\cdot N_{FA}}-\phi_{ACT,s}\right)+\exp\left(-\frac{F_{tot}}{f_{ACT}^{*}\cdot N_{FA}}+\phi_{ACT,c}\right)\right]\right\} \quad (7).$$

Of note, the integrin catch-slip bond and the F-actin catch-slip bond used in the current theoretical framework could be readily generalized to incorporate other molecular machineries residing in FA and the actin CSK that exhibit catch-slip bond behaviors. For example, Equ. (4) could also be applied directly to describe force-dependent catch-slip-like behaviors of vinculin[6-7], another FA protein. In addition, Equ. (7) could be used directly to describe force-dependent, catch-slip-like recruitment of actin-binding scaffold proteins, such as filamin and α-actinin[8-9], onto F-actin filaments, which could further modulate mechanical properties of actin stress fibers as in Equ. (8) below.

Muscle-like spontaneous contraction upon external force stimulation

Cell stretch-induced changes of CSK tension on stress fibers could be simulated using a contractile element (CE)-spring model[10-11] (**Supplementary Fig. 11**). Thus, to simulate cell

stretch on the SμPA, a mechanical model was developed that comprised a spring representing a PDMS micropost in series with another spring and a CE representing actin stress fiber containing myosin motor proteins arranged in parallel. The effective spring constant K_{eff} of the model was given by $1/K_{eff} = 1/K_{post} + 1/K_{SF}$, where K_{post} and K_{SF} were the spring constants of the PDMS micropost and actin stress fiber, respectively. The total force F_{tot} was thus calculated as $F_{tot} = K_{eff}\left[L - \left(L_0 + \Delta L\right)\right]$, where L was the length of activated CE-spring assembly under external force, L_0 was the length of inactivated and tension-free CE-spring assembly, and ΔL was the length change driven purely by myosin motor protein activity. ΔL would be negative for shortening and positive for lengthening of actin stress fiber, respectively. Temporal evolution of F_{tot} was then calulcated as $dF_{tot}/dt = K_{eff}\left(dL/dt - d\Delta L/dt\right)$, where dL/dt was determined from cell stretches on the SμPA and $d\Delta L/dt$ was derived from a linear force-velocity relation simiplified from the *Hill*'s muscle model $F_{tot} = N_{MYO} f_{stall}\left[1 + \left(d\Delta L/dt\right)/v_0\right]$[3,12], where N_{MYO}, the number of myosin molecules on actin stress fiber, was assumed proportional to the total nubmer of actin monomers N_{ACT} ($N_{MYO} = cN_{ACT}$; c was a constant), f_{stall} was the myosin stall force, and v_0 was the equivlant sliding velocity of myosin. Together, the governing equation for spontaneous muscle-like contraction of actin stress fiber when $t > 0$ was expressed as

$$\frac{dF_{tot}}{dt} = \left(K_{post}^{-1} + K_{SF}^{-1}\right)^{-1} \cdot \left[\frac{dL}{dt} - v_o\left(\frac{F_{tot}}{c \cdot f_{stall} \cdot N_{ACT}} - 1\right)\right] \qquad (8).$$

Equations (4), (7), and (8) formed a complete set of equations needed for calculating temporal variations of FA size N_{FA}, the total number of actin monomers in actin stress fiber N_{ACT}, and the total force exerted on FA F_{tot}, when responding to external cell stretches.

Steady-state solution of the biophysical model for cells at the ground state

The ordinary differential equations governing force dependent dynamic evolutions of FA size N_{FA} (Equ. (4)) and the total number of actin monomers N_{ACT} (Equ. (7)) allowed us to calculate steady-state solutions describing the relationship between CSK tension, FA size, and actin stress fiber for cells at the ground state.

Setting $dN_{FA}/dt = 0$ in Equ. (4) allowed calculations of steady-state solutions for Equ. (4) as

$$F_{tot} = N_{FA} \cdot f_{FA}^{*} \left\{ \phi_{FA,\max} + \cosh^{-1}\left[\frac{\gamma_{FA}\left(N_{FA}^{tot} - N_{FA}\right)}{2\alpha_{FA} \cdot N_{FA}} \right] \right\} \tag{9}$$

and

$$F_{tot} = N_{FA} \cdot f_{FA}^{*} \left\{ \phi_{FA,\max} - \cosh^{-1}\left[\frac{\gamma_{FA}\left(N_{FA}^{tot} - N_{FA}\right)}{2\alpha_{FA} \cdot N_{FA}} \right] \right\} \tag{10}$$

, where $\alpha_{FA} = \exp(\phi_{FA,c}/2 - \phi_{FA,s}/2)$ and $\phi_{FA,\max} = \left(\phi_{FA,c} + \phi_{FA,s}\right)/2$. Equ. (9) and Equ. (10) plotted as dashed and solid curves, respectively, in **Supplementary Fig. 16a** with N_{FA} and F_{tot} as the *x*- and *y*-axes, respectively, divided the plot into three different regions, where dN_{FA}/dt was positive in the area enclosed by the two curves (*region i*) and negative outside the area (*region ii* and *iii*). Individual FAs with a transient state falling in *region i* and *ii* would be capable of restoring their equilibrium states on the solid curve by recruiting and clustering new

FA proteins and modulated FA disassembly, respectively. In contrast, individual FAs in *region iii* were unstable and would rapidly disassemble and be completely dissolved. Together, Equ. (10) provided a stable steady-state solution and was used for theoretical calculations of steady-state conditions under different drug treatment conditions (**Supplementary Fig. 16b-e**).

Of note, when external perturbations were mild, CSK tension and FA were capable of self-adaptation to restore their stable equilibrium states in a quasi-static manner. Here, stability of self-adaptation of CSK tension and FA was limited by the end point of theoretical curves calculated from Equ. (10), beyond which stable steady-state solutions became unavailable and FA would undergo rapid disassembly.

Similarly, a stable steady-state solution for Equ. (7) was obtained as

$$F_{tot} = N_{FA} \cdot f_{ACT}^{*} \left\{ \phi_{ACT,\max} - \cosh^{-1}\left[\frac{\gamma_{ACT}\left(N_{ACT}^{tot} - N_{ACT}\right)}{2\alpha_{ACT} \cdot N_{ACT}} \right] \right\} \qquad (11)$$

, where $\alpha_{ACT} = \exp(\phi_{ACT,c}/2 - \phi_{ACT,s}/2)$ and $\phi_{ACT,\max} = \left(\phi_{ACT,c} + \phi_{ACT,s}\right)/2$. Equ. (10) and Equ. (11) together defined stablilty of the FA-CSK tension system and provided stable steady-state solutions for N_{FA}, N_{ACT}, and F_{tot} at ground states.

Determination of model parameters for untreated cells

Equations (10) and (11) provided a stable solution space for N_{FA}, N_{ACT}, and F_{tot} at ground states. Parameters including N_{FA}^{tot} and N_{ACT}^{tot} were selected to ensure F_{tot} covering a physiologically relevant range from 0 - 10 nN as observed in experiments with REF-52 fibroblasts. Parameters for integrin and F-actin catch-slip bonds including f_{FA}^{*}, $\phi_{FA,s}$, $\phi_{FA,c}$, f_{ACT}^{*}, $\phi_{ACT,s}$, and $\phi_{ACT,c}$ were determined by fitting experimental data reported previously[1-2] using Equ.

(3) and Equ. (6) with $k_{FA,o}$ and $k_{ACT,o}$ set to 1 s^{-1} (**Fig. 2k**, **Supplementary Fig. 12** and **Supplementary Table 1**). K_{post} was determined using finite element analysis, and K_{post} = 7.2 nN μm^{-1}. K_{SF} was estimated by assuming actin stress fibers as solid ropes with a rope length of 60 μm (L; $t < 0$), a rope diameter of 1 μm, and a modulus of 12 kPa[13-14]. Myosin stall force f_{stall} was selected to match experimental results reported previously[15], and the equivalent sliding velocity of myosin molecules v_o was set as 1/10 of the value measured for a single myosin molecule sliding on unloaded F-actin[16], to compensate discontinuous myosin sliding on F-actin (power stroke duty ratio). Value of the constant c in Equ. (8) was determined by fitting quasi-static values of the total force F_{tot} exerted on FA obtained experimentally with REF-52 fibroblasts. A complete list of model parameters was provided in **Supplementary Table 1**.

Theoretical validation of the indispensability of catch-slip bonds and myosin motor activity

To examine whether integrin catch-slip bond would be indispensable for theoretical recapitulation of subcellular rheostasis of CSK tension and FA, Equ. (4) was modified to remove the catch-bond portion of the integrin catch-slip bond as

$$\frac{dN_{FA}}{dt} = k_{FA,o}\left[\gamma_{FA}\left(N_{FA}^{tot} - N_{FA}\right) - N_{FA}\cdot\exp\left(\frac{F_{tot}}{f_{FA}^{*}\cdot N_{FA}} - \phi_{FA,s}\right)\right] \quad (12).$$

Equations (7), (8), and (12) formed a complete set of equations needed for calculating temporal evolutions of FA size N_{FA}, the total number of actin monomers in actin stress fiber N_{ACT}, and the total force exerted on FA F_{tot}, when responding to external cell stretches with pure slip bonds between integrin and fibronectin.

In distinct contrast to the stable steady-state solution in **Supplementary Fig. 16a** that allowed spontaneous restoration of CSK tension and FA to their stable equilibrium states under small perturbations, the only steady-state solution to Equ. (12) expressed as

$$F_{tot} = N_{FA} \cdot f_{FA}^{*} \left\{ \phi_{FA,s} + \ln \left[\frac{\gamma_{FA} \left(N_{FA}^{tot} - N_{FA} \right)}{N_{FA}} \right] \right\} \tag{13}$$

was unstable for majority of its solution space (**Supplementary Fig. 18a**). Specifically, the steady-state solution curve descrbied by Eq. (13) was biphasic and divided a two-dimensional surface with N_{FA} and F_{tot} as the *x*- and *y*-axes, respectively, into three different regions, where dN_{FA}/dt was positive underneath the curve (*region i*) and negative above the curve (*region ii* and *region iii*). Individual FAs with a transient state falling into *region i* and *region ii* would approach equilibrium states on the solid portion of the theoretical curve where FA size were unrealistically large and FA size and CSK tension became negatively correlated (contradictory to experimental observations). FAs on the rest part of the steady-state solution curve (dashed line) were unstable: they would either be completely dissolved or grow to its maximum size when perturbed to fall into *region iii* or *region i*, respectively. Such hypersensitivity of the FA-CSK tension system without catch bonds was also revealed in simulations of dynamic responses of CSK tension and FAs upon cell stretch. Majority of FAs disassembled instantaneously upon cell stretch, while those survived in the initial phase grew to its maximum regardless of CSK tension force, contradictory to experimental observations of subcellular rheostasis of CSK tension and FA (**Supplementary Fig. 18b,c**).

The necessity of myosin motor activity for subcellular rheostasis of CSK tension and FA was investigated by removing it from Equ. (8), resulting in a modified Equ. (8) with only elastic

properties as $dF_{tot}/dt = \left(K_{post}^{-1} + K_{SF}^{-1}\right)^{-1} \cdot dL/dt$. Simulation results using this modified equation recapitulated reinforcements of both CSK tension and FA in *Phase I* of the homeostatic response, but failed to predict subcellular rheostasis in *Phase II* of the homeostatic response (**Supplementary Fig. 18d-f**).

Theoretical modeling was computed using MatLab with a custom-written code, which is available upon request.

SUPPLEMENTARY FIGURES AND FIGURE CAPTIONS

Supplementary Figure 1

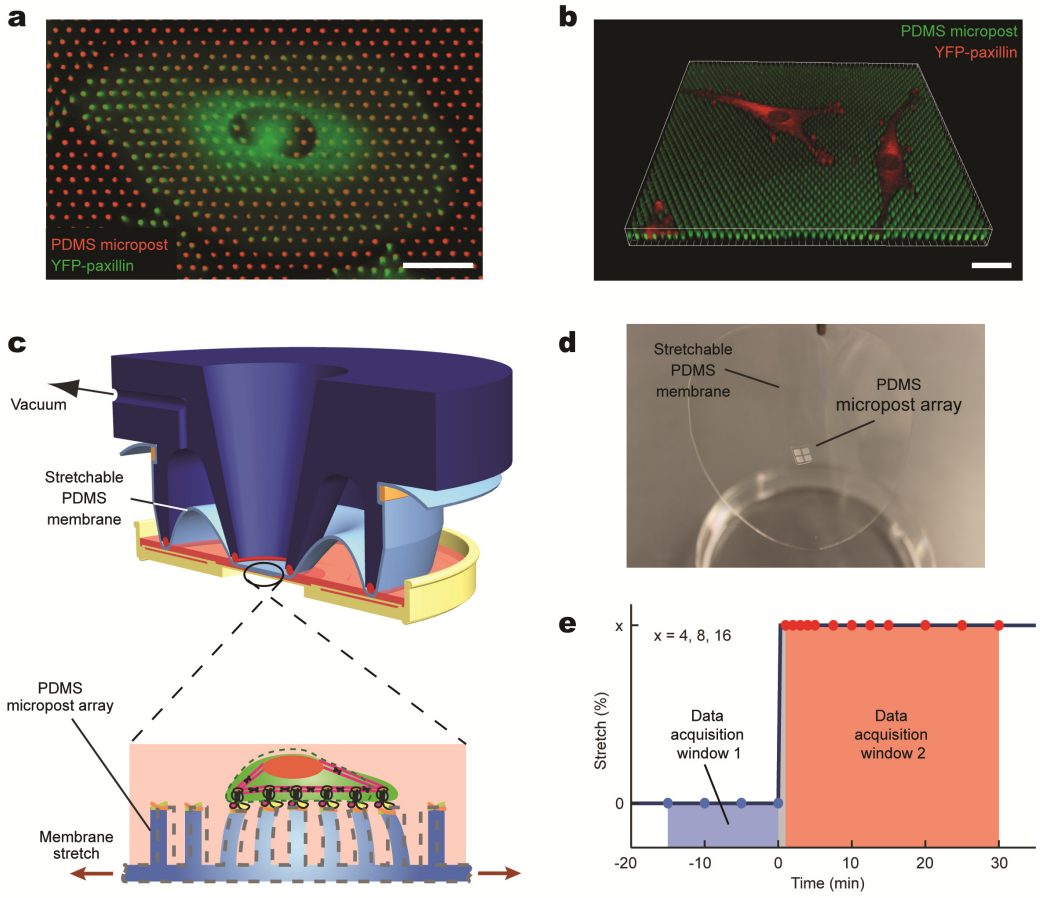

Supplementary Figure 1. Experimental setup using stretchable micropost array (SμPA) to apply equibiaxial stretch to live single cells while simultaneously monitoring dynamic responses of subcellular cytoskeleton (CSK) tension and focal adhesion (FA). (**a**) Representative fluorescence microscopy image showing a single REF-52 cell expressing YFP-paxillin seeded on the SμPA. Scale bar, 20 μm. (**b**) Reconstructed three-dimensional confocal fluorescence microscopy image showing single REF-52 cells expressing YFP-paxillin on the SμPA. Note that only the top portion of PDMS microposts was shown. Scale bar, 20 μm. (**c**) Schematic of a custom-made, vacuum-driven cell stretching device (CSD), which contained a circular viewing aperture surrounded by a vacuum chamber. The SμPA was inverted before mounted onto the

CSD with the PDMS micropost array centered on the viewing aperture to permit direct visualization of live cells and PDMS microposts under microscopy. The CSD was placed inside a glass-bottom dish to facilitate high-resolution live-cell imaging. The CSD was activated for cell stretch by applying vacuum to draw periphery of the PDMS base membrane into the vacuum chamber, causing the central area of SμPA holding the PDMS micropost array to stretch equibiaxially. Stretch magnitude was determined *in situ* by utilizing regularly positioned PDMS microposts as fiduciary markers. (**d**) Photo showing SμPA before mounted onto the CSD. (**e**) Static equibiaxial stretch protocol in conjunction with real-time, live-cell imaging to monitor dynamic responses of CSK tension and FA size. Prior to cell stretch, fluorescence microscopy images of micropost tops and FAs were recorded every 5 min for a total of 15 min (t = -15, -10, -5, and 0 min; data acquisition window 1). At the onset of stretch when t = 0 min, a rapid step increase of stretch (with a stretch magnitude of 4%, 8%, or 16%) was applied and held constant for another 30 min. Fluorescence microscopy images of micropost tops and FAs were acquired at t = 1, 2, 3, 4, 5, 7.5, 10, 12.5, 15, 20, 25, and 30 min (data acquisition window 2).

Supplementary Figure 2

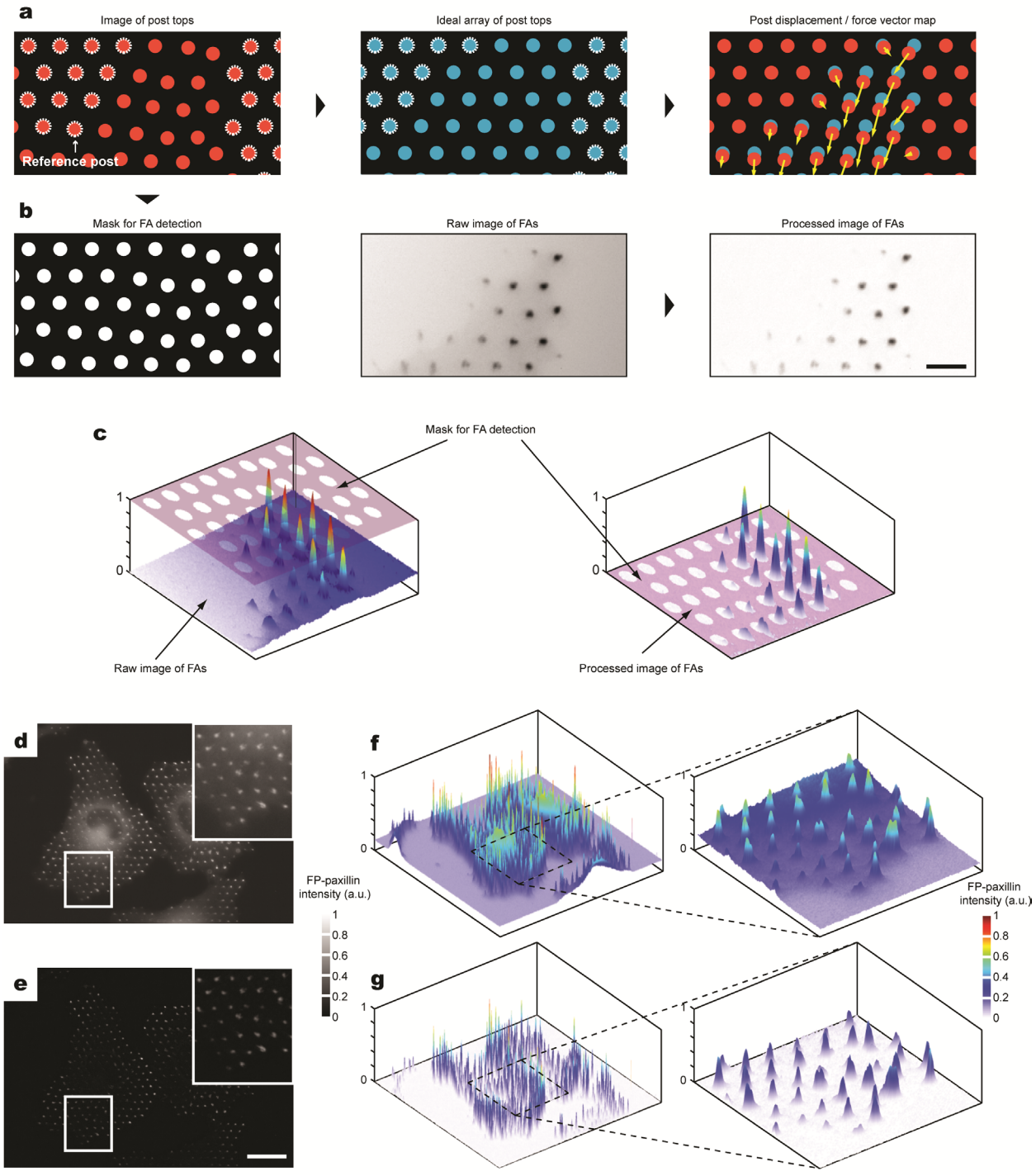

Supplementary Figure 2. Quantitative image analysis of subcellular cytoskeleton (CSK) tension and focal adhesion (FA). (**a-c**) Image analysis to quantify CSK tension (**a**) and FA (**b**) in a spatially registered manner. Free-standing, unbent microposts without cell attachment (marked

by dashed white circles in **a**) were selected as reference posts to generate an ideal force-free post array (blue; *middle*, **a**). Displacements of post tops from their unbent positions were then quantified and multiplied by the micropost spring constant to obtain CSK tension exerted on microposts (yellow force vectors; *right*, **a**). Fluorescence microscopy image of micropost tops was converted into a binary image as a mask for FA detection (*left*, **b**). Local background fluorescence in raw fluorescence microscopy images of FP-paxillin was subtracted using morphological opening (*middle* and *right*, **b**). Scale bar, 5 μm. (**c**) Illustration showing 3-D colorimetric heat maps of FP-paxillin before (*left*) and after (*right*) background fluorescence subtraction and one-to-one spatial registration of each FA to individual single micropost using the image of micropost tops as a FA detection mask. (**d-g**) Subtraction of background fluorescence using a morphological opening algorithm to extract FP-paxillin intensity for each individual FA. Representative fluorescence microscopy images of FP-paxillin (**d&e**) and corresponding 3-D colorimetric heat maps (**f&g**) before (**d&f**) and after (**e&g**) background fluorescence subtraction. Scale bar, 20 μm.

Supplementary Figure 3

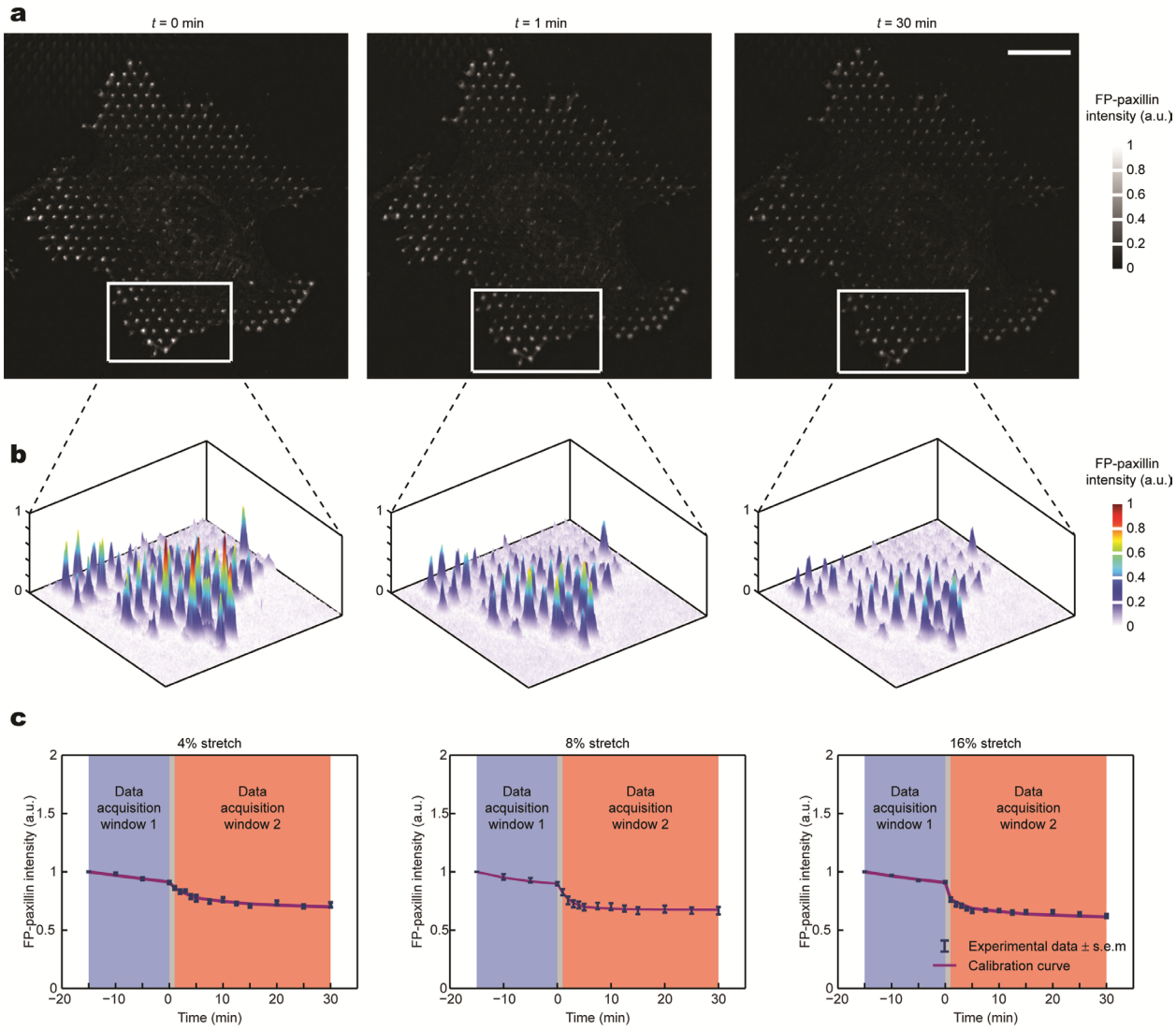

Supplementary Figure 3. Compensation of fluorescence quenching due to photobleaching and light path variation caused by cell stretch. To quantify fluorescence quenching, FP-paxillin expressing cells seeded on the SμPA were fixed before assayed using the same static equibiaxial stretch protocol shown in **Supplementary Fig. 1e**. (**a&b**) Representative fluorescence microscopy images (after background fluorescence subtraction) of FP-paxillin (**a**) and corresponding 3-D colorimetric heat maps (**b**) before (t = 0 min) and after the onset of 8% static equibiaxial stretch (t = 1 min and t = 30 min), showing noticeable decay of fluorescence intensity

due to non-specific effects of fluorescence quenching caused by photobleaching and light path variation resulted from cell stretch. (**c**) Calibration curves for fluorescence quenching of YFP-paxillin intensity during cell stretch assays at the stretch levels of 4%, 8%, and 16% as indicated. Under each stretch level, normalized whole-cell YFP-paxillin intensity as a function of time was best fitted with two exponential functions (purple curves), serving as a calibration curve for compensating fluorescence quenching for live-cell assays. Note that whole-cell YFP-paxillin intensity was normalized to values obtained at the beginning of cell stretch assays (t = -15 min). Data represents the mean ± s.e.m with n = 10.

Supplementary Figure 4

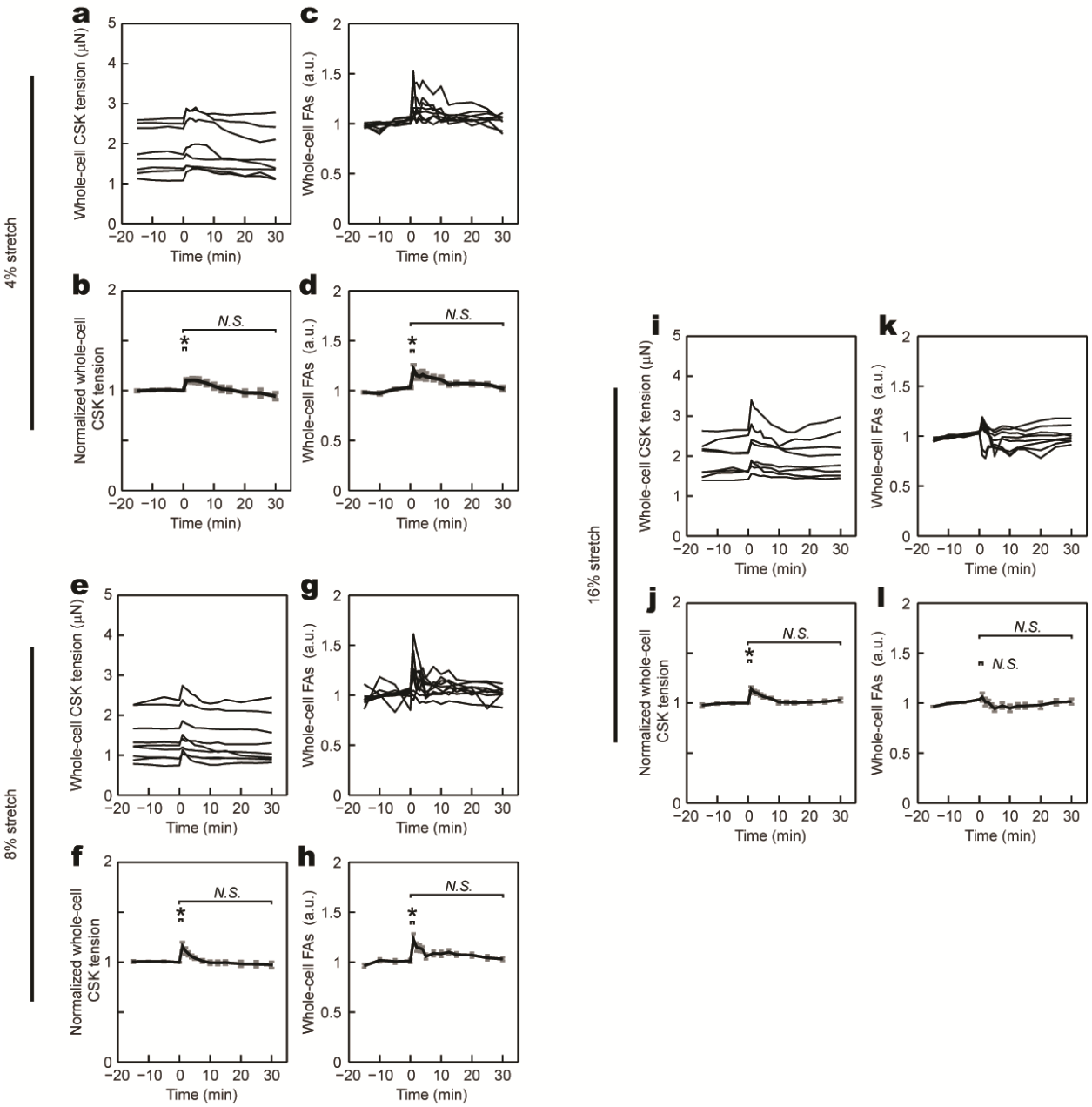

Supplementary Figure 4. Single-cell mechanical homeostasis. REF-52 cells were subjected to 4% (**a-d**), 8% (**e-h**), and 16% (**i-l**) static equibiaxial stretches. Temporal evolutions of whole-cell CSK tension and FA size were plotted for individual single cells (whole-cell CSK tension: **a**, **e**, **i**; whole-cell FA size: **c**, **g, k**) as well as corresponding averages of normalized data (whole-cell CSK tension: **b**, **f**, **j**; whole-cell FA size: **d**, **h**, **l**). For normalization, data for each single cell was

normalized to ground-state values at $t = 0$ min. Averaged results were plotted as mean ± s.e.m, with $n = 8, 10, 8$ cells for 4%, 8%, and 16% stretches, respectively.

Supplementary Figure 5

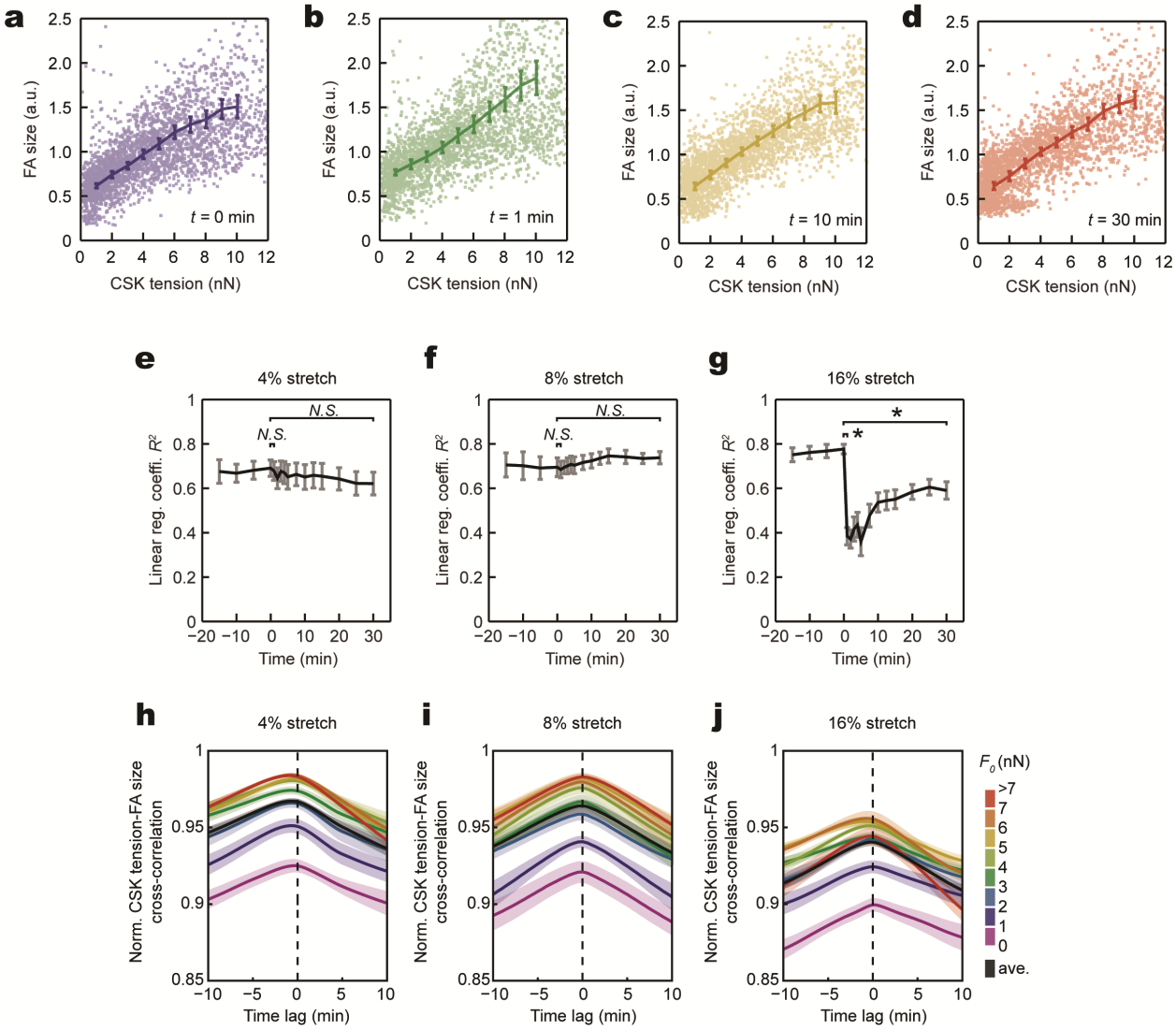

Supplementary Figure 5. Dynamic correlation and synchronization of subcellular cytoskeleton (CSK) tension and focal adhesion (FA) during single-cell mechanical homeostasis. (**a-d**) Linear correlation analysis between subcellular CSK tension and FA size for single REF-52 cells before (t = 0 min; **a**) and after (t = 1 min, 10 min, and 30 min; **b-d**) the onset of 8% static equibiaxial stretch. Each data point represents an individual FA, and data was pooled from 10 single REF-52 cells with a total of over 2,500 FAs. Data trends were plotted as moving averages (line curves) ± s.e.m, with n = 10 cells. (**e-g**) Linear regression coefficients R^2 calculated from best linear

fitting of paired FA size - CSK tension data were plotted as a function of time for 4% (**e**), 8% (**f**), and 16% (**g**) stretches. Linear correlation between subcellular CSK tension and FA size was well maintained throughout the entire single-cell homeostatic responses under 4% and 8% stretches. For 16% stretch, linear regression coefficients R^2 decreased sharply right after cell stretch before recovering gradually over the next 30 min. Data represents the mean ± s.e.m, with n = 8, 10, 8 for 4%, 8%, and 16% stretches, respectively. P-values were calculated using student's paired sample t-test comparing the data before (t = 0 min) and after (t = 1 min, 30 min) cell stretch. *N.S.*, statistically not significant and $P > 0.05$. *, $P < 0.05$. (**h-j**) Cross-correlation analysis of temporal coordination between subcellular CSK tension and FA size in response to 4% (**h**), 8% (**i**), and 16% (**j**) stretches. Results were grouped based on ground-state values of CSK tension before cell stretch (F_0 at t = 0 min). Maximums of normalized cross-correlation between CSK tension and FA size for each FA subgroups were all around or above 0.9, supporting the prominent temporal synchronization between CSK tension and FA size in response to 4% - 16% cell stretches. Data represents the mean (solid curves) ± s.e.m (shaded area), and n = 8, 10, 8 for 4%, 8%, and 16% stretches, respectively.

Supplementary Figure 6

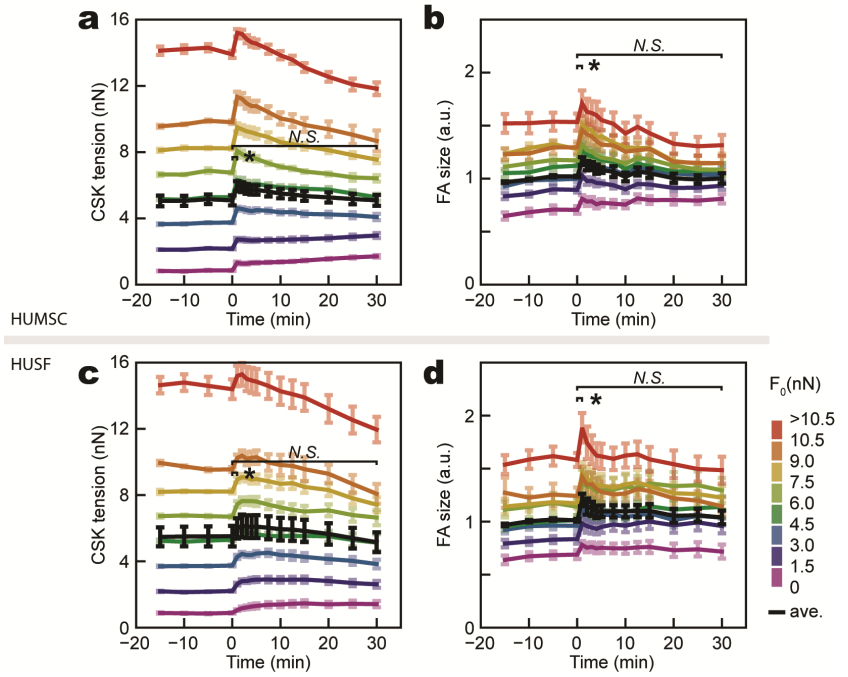

Supplementary Figure 6. Single-cell mechanical homeostasis in human mesenchymal stem cells (HUMSCs; **a&b**) and human skin fibroblasts (HUSFs; **c&d**) under 8% static equibiaxial stretch was driven collectively by subcellular rheostasis of cytoskeleton (CSK) tension and focal adhesion (FA). Heterogeneous rheostatic paths for subcellular CSK tension (**a&c**) and FA (**b&d**) were plotted for FA subsets grouped based on ground-state values of CSK tension F_0 at $t = 0$ min. Average result from each subset was plotted using the rainbow spectrum (from *purple* to *red*). Whole-cell average responses were included for referencing single-cell homeostasis (*black*). Data represents the mean ± s.e.m with $n = 10$ cells. *P*-values were calculated using student's paired sample *t*-test comparing data before ($t = 0$ min) and after ($t = 1$ or 30 min) stretch. *N.S.*, statistically not significant and $P > 0.05$. *, $P < 0.05$.

Supplementary Figure 7

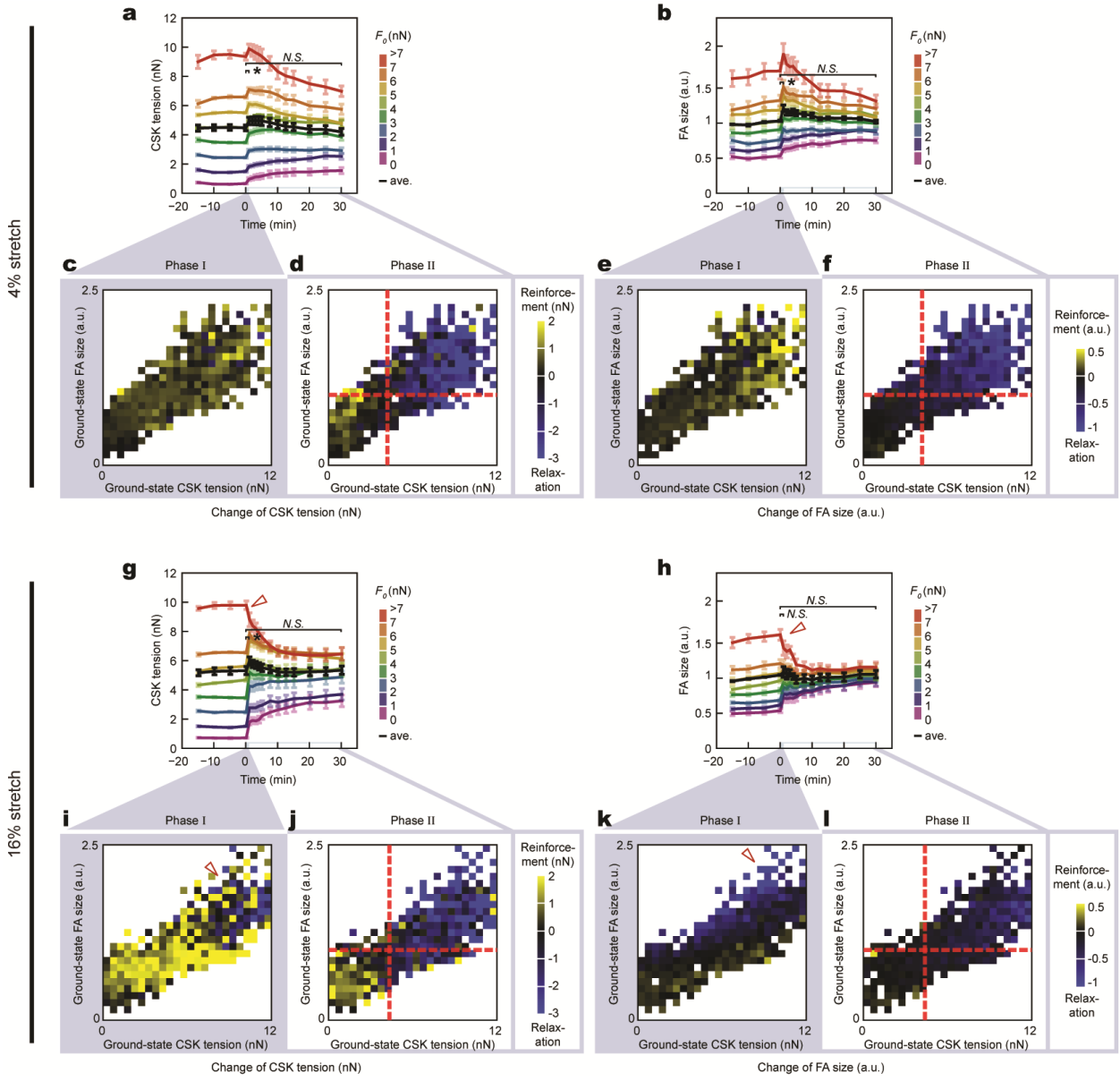

Supplementary Figure 7. Subcellular cytoskeleton (CSK) tension and focal adhesion (FA) followed distinct mechanosensitive rheostasis to drive single-cell mechanical homeostasis for single REF-52 cells under 4% (**a-f**) and 16% (**g-l**) static equibiaxial stretches. (**a, b, g, h**) Heterogeneous rheostatic paths for subcellular CSK tension (**a**, **g**) and FA (**b**, **h**). Results were grouped into subsets based on ground-state CSK tension values F_0 at $t = 0$ min. Average result from each subset was plotted using the rainbow spectrum (from *purple* to *red*). Whole-cell

average responses (*black*) were included as a reference. Data represents the mean ± s.e.m with n = 8 for both 4% and 16% stretches. P-values were calculated using student's paired sample t-test comparing data before (t = 0 min) and after (t = 1 or 30 min) stretch. *N.S.*, statistically not significant and $P > 0.05$. *, $P < 0.05$. (**c-f, i-l**) Dependence of subcellular rheostasis on ground-state values of CSK tension and FA size. Changes in CSK tension (**c&d**, **i&j**) and FA size (**e&f**, **k&l**) during *Phase I* (t = 0 - 1 min; **c**, **e**, **i**, **k**) and *phase II* (t = 1 - 30 min; **d**, **f**, **j**, **l**) were color-coded in two-dimensional CSK tension - FA size diagrams obtained at t = 0 min showing ground-state values of CSK tension and FA size. Red dashed lines in **d**, **f**, **j**, and **l** marked average ground-state values of CSK tension and FA size as well as a transition boundary between reinforcement and relaxation for subcellular rheostasis of CSK tension (**d**, **j**) and FA size (**f**, **l**) during *Phase II*. Hollow red arrowheads indicated damped reinforcement of CSK tension and FA size in *Phase I*.

Supplementary Figure 8

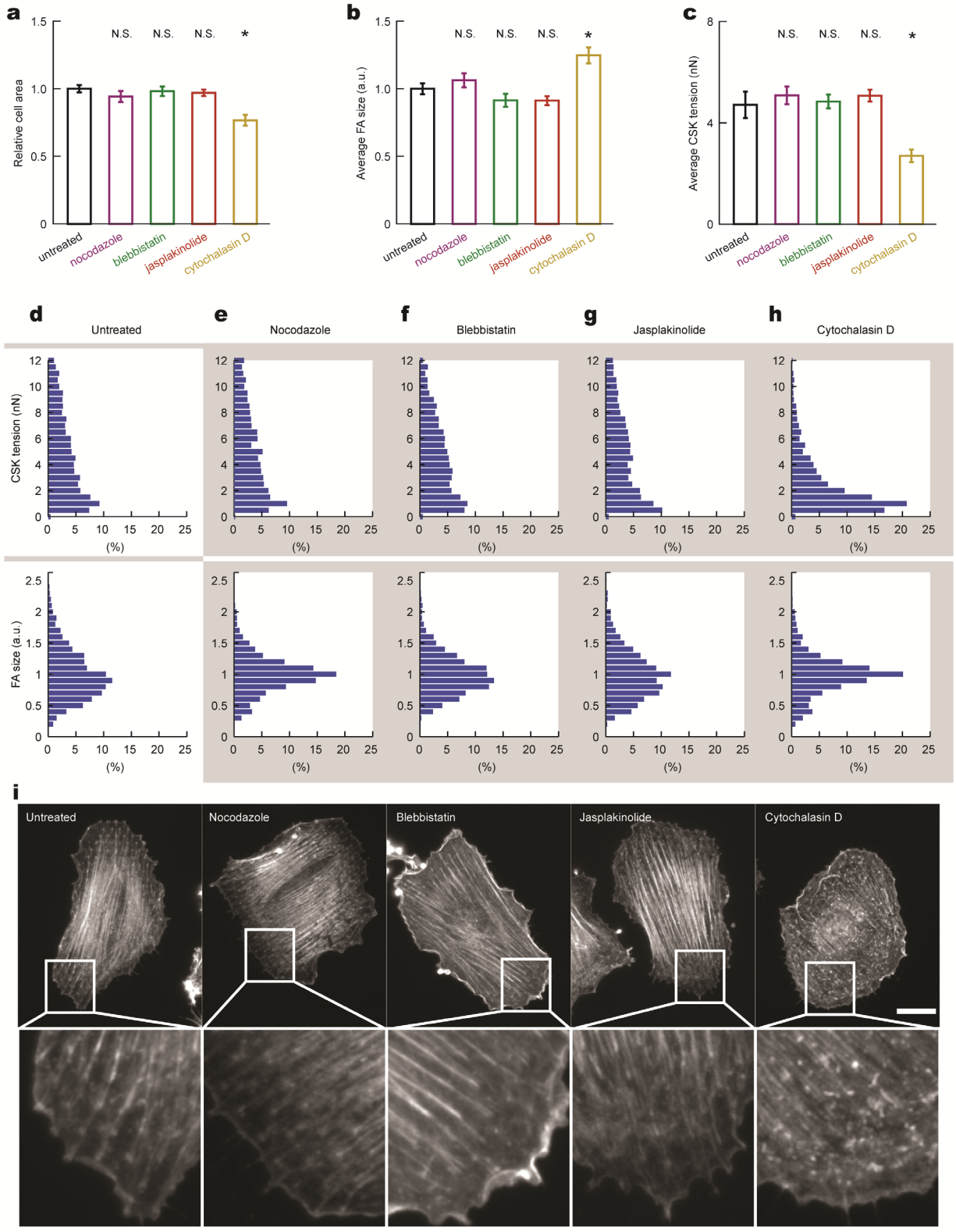

Supplementary Figure 8. Effect of treatments with low-dosage pharmacological small-molecule inhibitors on cell spread area (**a**), focal adhesion (FA) formation (**b**, **d-h**), cytoskeleton (CSK) tension (**c**, **d-h**), and actin CSK architecture (**i**) for REF-52 cells. Drug dosages: nocodazole, 50 nM; blebbistatin, 10 μM; jasplakinolide, 10 nM; cytochalasin D, 200 nM. Data in **a** and **b** was normalized to values obtained for untreated controls. Data represents the mean ± s.e.m with $n = 10$. *P*-values were calculated using student's paired sample *t*-test comparing drug treated cells with untreated control. *N.S.*, statistically not significant and $P > 0.05$. *, $P < 0.05$. (**d-h**) Distribution of subcellular CSK tension (*top*) and FA size (*bottom*) for untreated and drug-treated REF-52 cells as indicated. For each condition, data from 10 cells and over 2,000 FAs was pooled and analyzed. (**i**) Representative fluorescence microscopy images showing effects of small-molecule inhibitors on the actin CSK architecture of REF-52 cells. Images at the bottom are magnifications of the boxed regions in the top images. REF-52 cells seeded on the SμPA were fixed and stained with fluorescently labeled phalloidin. Untreated REF-52 cells and those treated with low dosages of nocodazole, blebbistatin, and jasplakinolide were all well spread with prominent, highly organized actin stress fibers. Compared to untreated control, REF-52 cells treated with cytochalasin D had smaller cell spreading and less organized and somewhat punctuated actin filaments. Nonetheless, we should note that there were still plenty visible actin stress fibers connected to FAs with measurable CSK tension. Scale bar, 20 μm.

Supplementary Figure 9

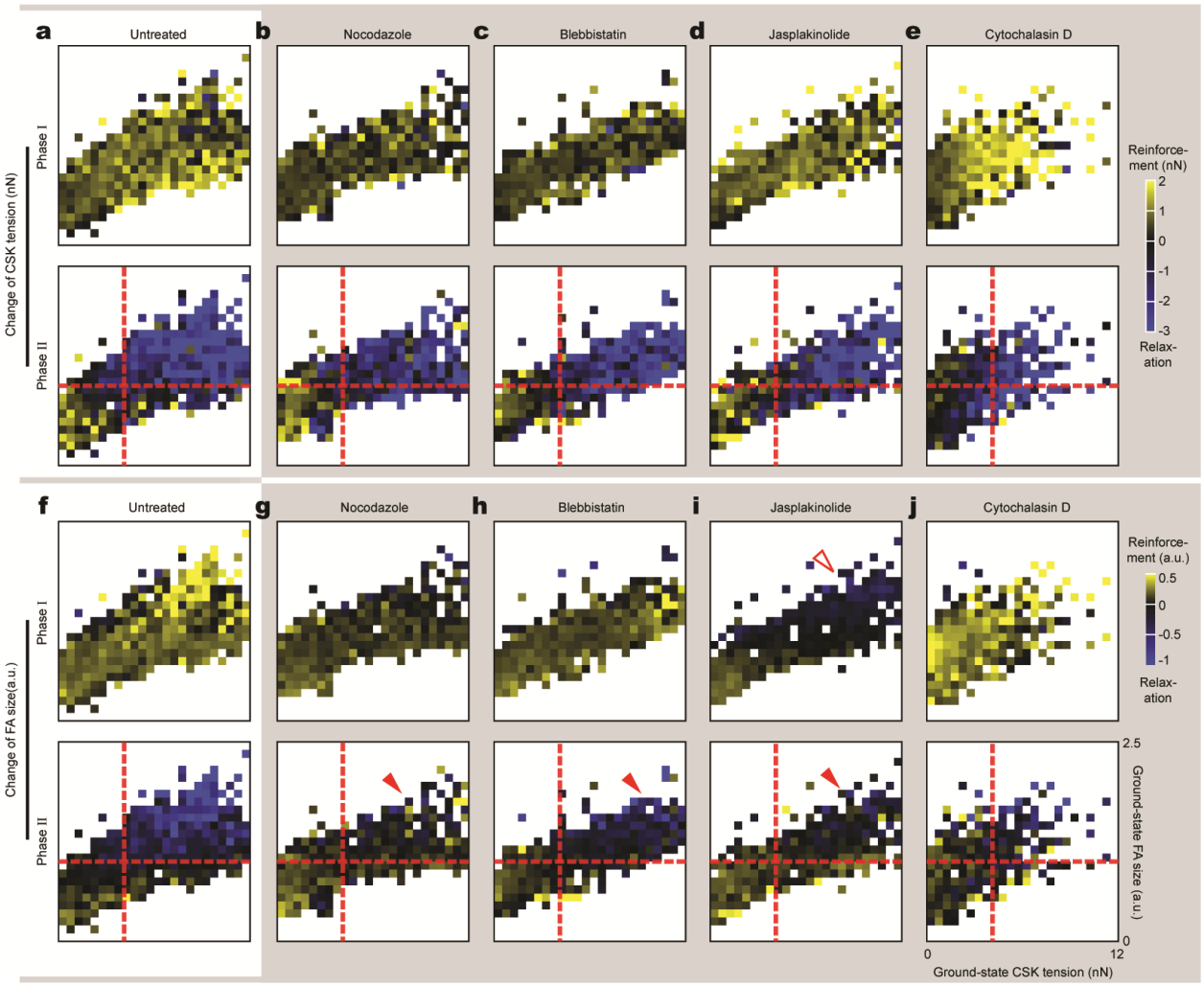

Supplementary Figure 9. Dependence of subcellular rheostasis on the CSK integrity. For both untreated and drug-treated REF-52 cells, changes of CSK tension (**a-e**) and FA size (**f-j**) during *Phase I* (*top*; t = 0 - 1 min) and *Phase II* (*bottom*; t = 1 - 30 min) of the mechanical homeostatic response were plotted as colorimetric diagrams showing ground-state values of CSK tension and FA size obtained at t = 0 min. Red dashed lines marking the average of ground-state values of CSK tension and FA size for untreated cells were included as references to illustrate changes in the mechanosensitive rheostatic patterns upon treatments with small-molecule inhibitors. Hollow red arrowheads indicated damped FA strengthening in *Phase I*, whereas solid red

arrowheads marked largely abolished FA relaxation in *Phase II*. Under each condition, data from 10 cells was pooled and analyzed.

Supplementary Figure 10

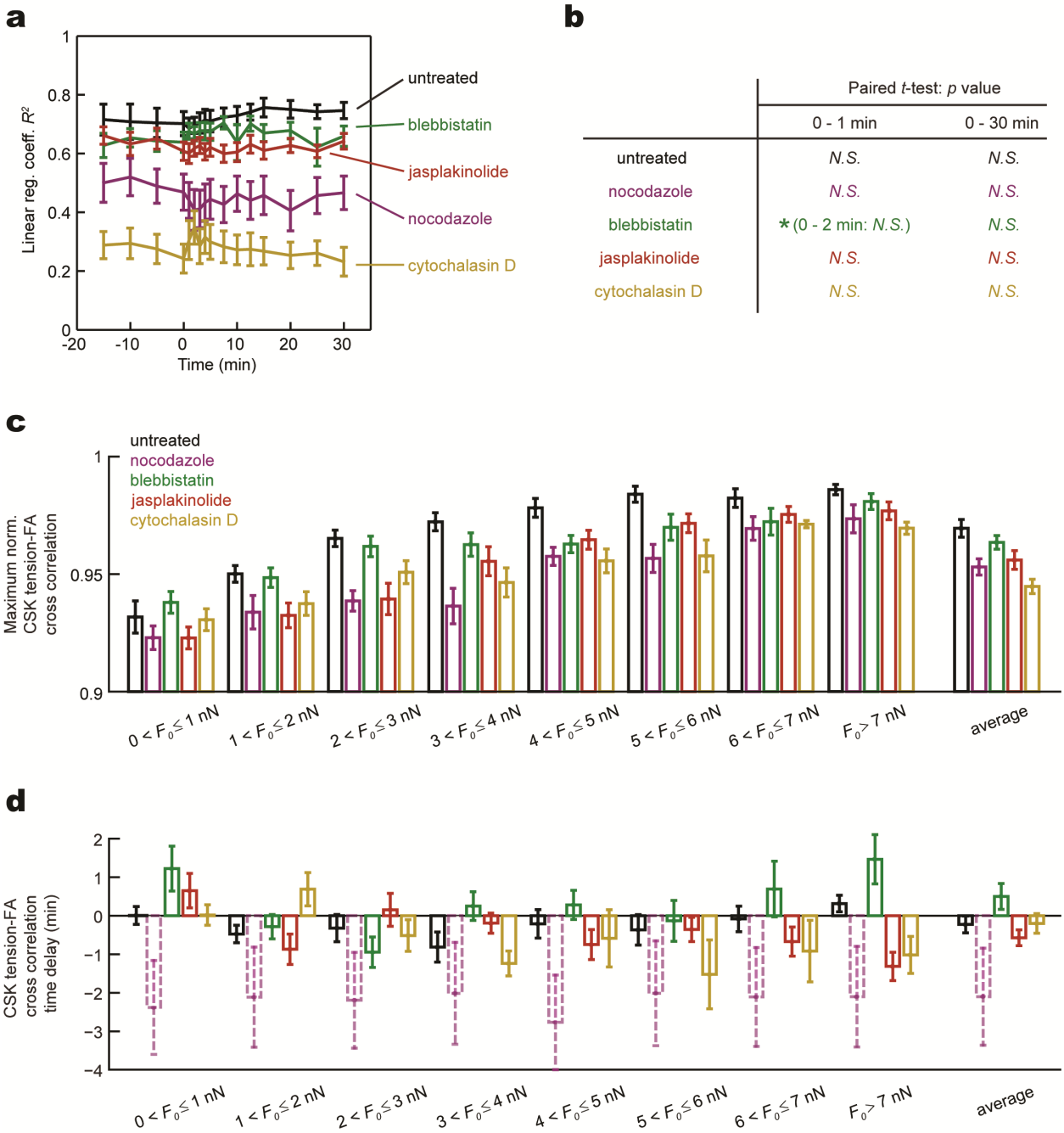

Supplementary Figure 10. Effects of small-molecule inhibitors on correlation (**a&b**) and synchronization (**c&d**) of subcellular cytoskeleton (CSK) tension and focal adhesion (FA) in REF-52 fibroblasts during homeostatic processes in response to 8% static equibiaxial stretch. (**a&b**) Linear regression coefficients R^2 calculated from best linear fitting of paired FA size -

CSK tension data were plotted as a function of time for both untreated and drug-treated cells as indicated. Data represents the mean ± s.e.m with $n = 10$. In **b**, P-values were calculated using student's paired sample t-test comparing R^2 values between $t = 0$ min and $t = 1$ min or between $t = 0$ min and $t = 30$ min. *N.S.*, statistically not significant and $P > 0.05$. *, $P < 0.05$. (**c&d**) Temporal synchronization between CSK tension and FA determined by cross-correlation analysis. Bar plot in **c** plotted maximum normalized cross-correlation between CSK tension and FA size and its dependence on ground-state values of CSK tension F_0 as well as drug treatment conditions as indicated. Maximums of normalized cross-correlation between CSK tension and FA size for all FA subgroups were > 0.9, supporting prominent temporal synchronization between CSK tension and FA size under different drug treatment conditions. Bar plot in **d** showed cross-correlation time delay between CSK tension and FA. Negative cross-correlation time delay suggested that FA responded more promptly than CSK tension and *vice versa*. Cross-correlation time delay data for the nocodazole treatment group was likely an artifact given the distinct difference between the data for CSK tension and FA size.

Supplementary Figure 11

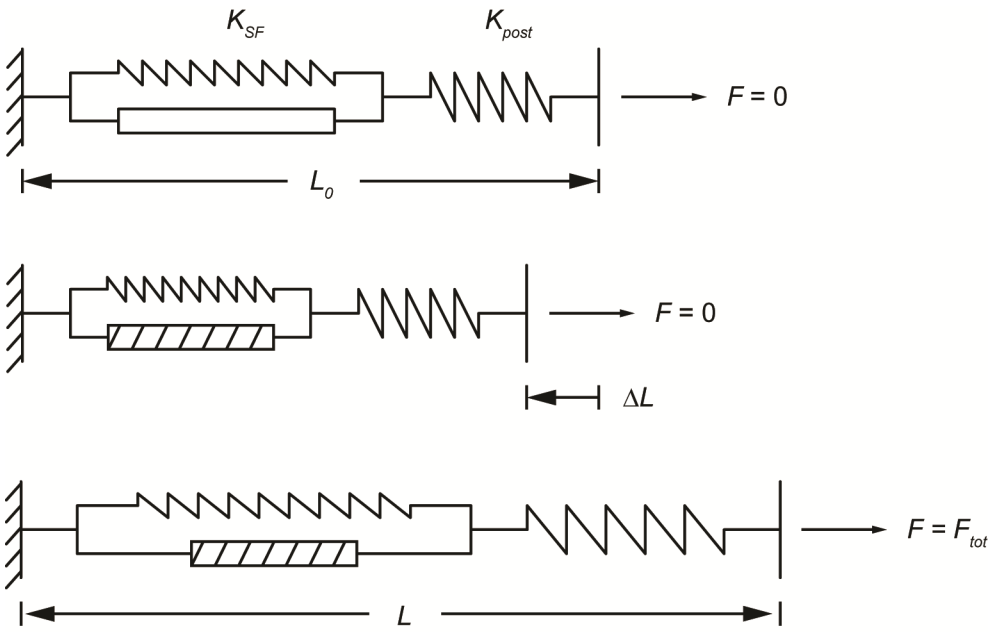

Supplementary Figure 11. Contractile element (CE)-spring model for analyzing muscle-like spontaneous contraction of the actin cytoskeleton (CSK) in response to external mechanical stimulation. The model comprised a spring representing a PDMS micropost (with a spring constant K_{post}) in series with another spring (with a spring constant K_{SF}) and a CE arranged in parallel representing atin stress fibers with myosin motor proteins. The model had a norminal length of L_0 when it was unloaded with the external load $F = 0$ and myosin motor proteins inactivated. Myosin motor protein activation would induced adaptive contraction of stress fibers with a change of length ΔL (negative for shortening and positive for lengthening) under a hypothetical load-free state. Under an external force F_{tot}, the model would reach its mechanical equilibrium with a new equilibrium length L.

Supplementary Figure 12

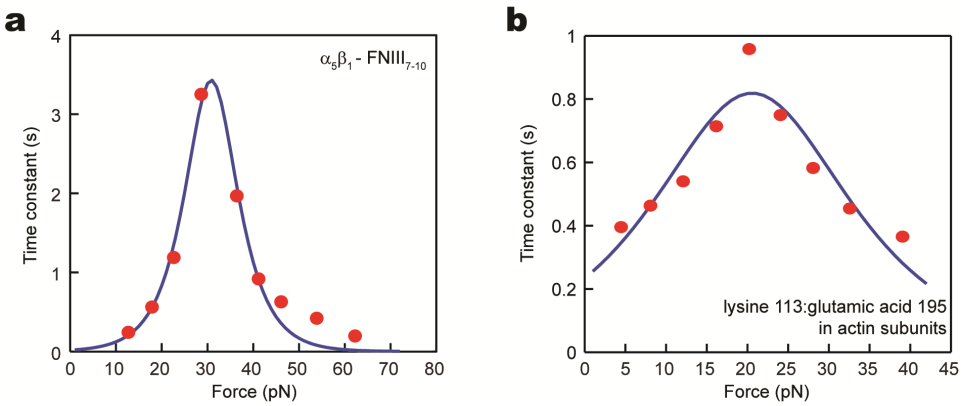

Supplementary Figure 12. Determination of catch-slid bond parameters. (**a**) Force - lifetime diagram of the catch-slip bond between $\alpha_5\beta_1$ integrin and FNIII$_{7\text{-}10}$. Two-pathway model (Equ. (3)) was used for fitting experimental data from Kong *et al.*[1] to determine catch-slip bond parameters between $\alpha_5\beta_1$ and FNIII$_{7\text{-}10}$, with best-fit parameters $\phi_{FA,s} = 7.78$, $\phi_{FA,c} = 4.02$, and $f_{FA}^* = 5.38$ pN. (**b**) Catch-slip bond between lysin113 and glutamic acid 195 in F-actin. Two-pathway model (Equ. (6)) was used for fitting experimental data from Lee *et al.*[2] to determine catch-slip bond parameters between lysin113 and glutamic acid 195 in F-actin, with best-fit parameters $\phi_{ACT,s} = 2.42$, $\phi_{ACT,c} = 1.43$, and $f_{ACT}^* = 10.68$ pN. Red dots in **a** and **b** were experimental results from Refs. [1] and [2], and navy curves were best-fitting curves generated from the two-pathway models.

Supplementary Figure 13

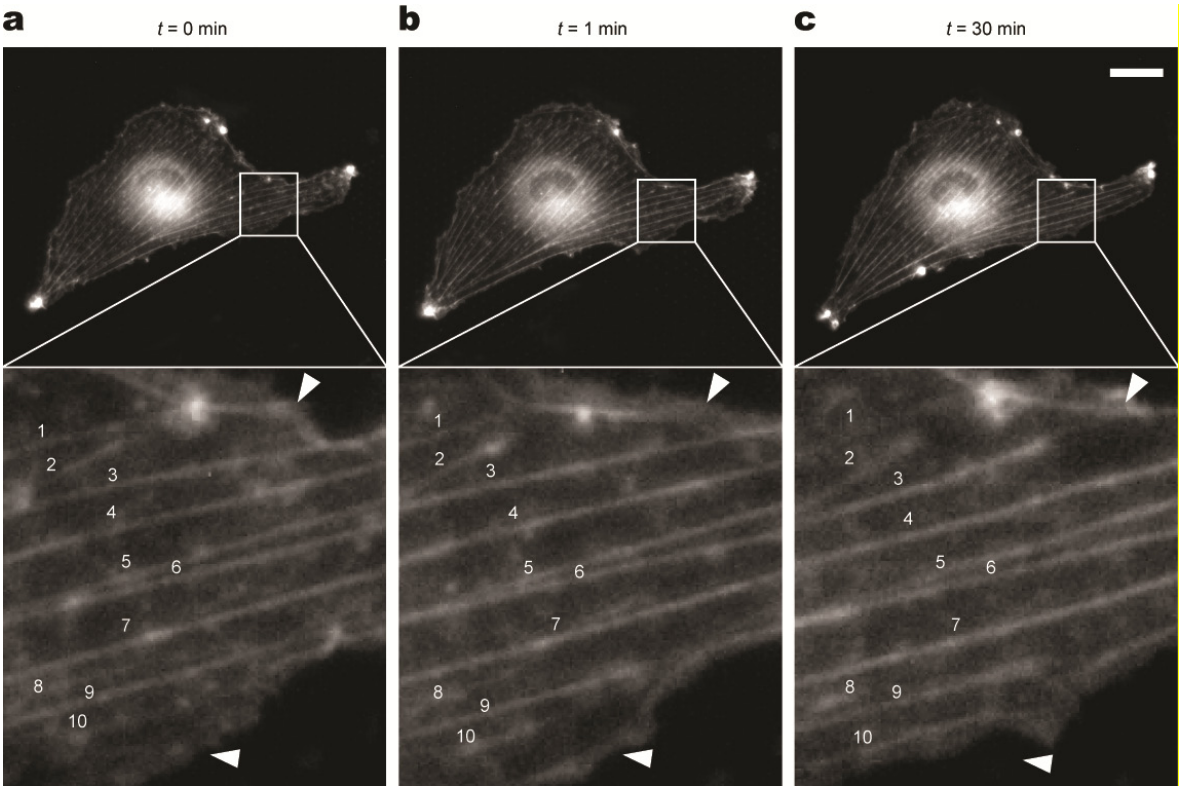

Supplementary Figure 13. Actin cytoskeleton (CSK) in REF-52 fibroblasts in response to 8% static equibiaxial stretch. REF-52 cells were transfected with CellLight Actin-RFP construct before assayed using the SμPA. Fluorescence microscopy images of RFP-actin were recorded before (t = 0 min, **a**) and after (t = 1 min, **b**; t = 30 min, **c**) the onset of cell stretch. Images at the bottom are magnifications of the boxed regions in the top images. Ten parallel actin stress fibers were selected and marked. During the entire cell stretch assay, there was no significant remodeling or reorientation of actin stress fibers in REF-52 fibroblasts, except mild shortening of fiber 3 and fiber 9 and elongation of fiber 10. White arrowheads marked areas at the cell periphery where cortical actin underwent remodeling.

Supplementary Figure 14

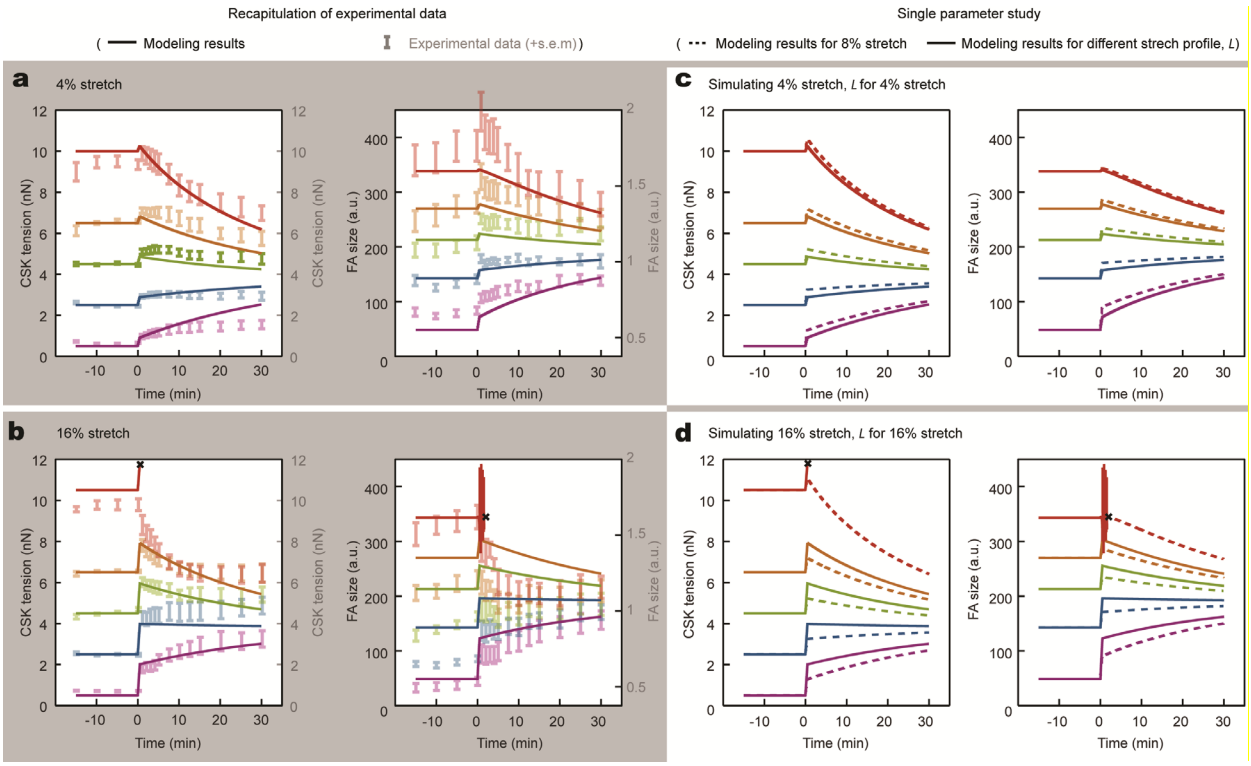

Supplementary Figure 14. Recapitulation of mechanosensitive rheostatic behaviors of subcellular cytoskeleton (CSK) tension and focal adhesion (FA) under 4% and 16% static equibiaxial stretches using the biophysical model. Theoretical calculations were conducted using model parameters determined through fitting ground-state values of REF-52 fibroblasts ($t \leq 0$ min) under 8% stretch, except that the stretch magnitude was set as 4% and 16% as indicated. (**a&b**) Theoretical calculations of rheostatic responses of CSK tension (*left*) and FA size (*right*) plotted against time (solid curves), agreeing reasonably well with experimental data (translucent error bars). (**c&d**) Single-parameter studies to elucidate the effect of stretch level on subcellular rheostasis. Modeling results for 4% (**c**) and 16% (**d**) stretches (solid curves) were plotted together with results from 8% stretch (dashed curves) for comparison. Black crosses in **b** and **d** marked where simulations became divergent, leading to unstable solutions and implying instability of FAs (see discussions in **Biophysical modeling** and **Supplementary Fig. 16a**).

Supplementary Figure 15

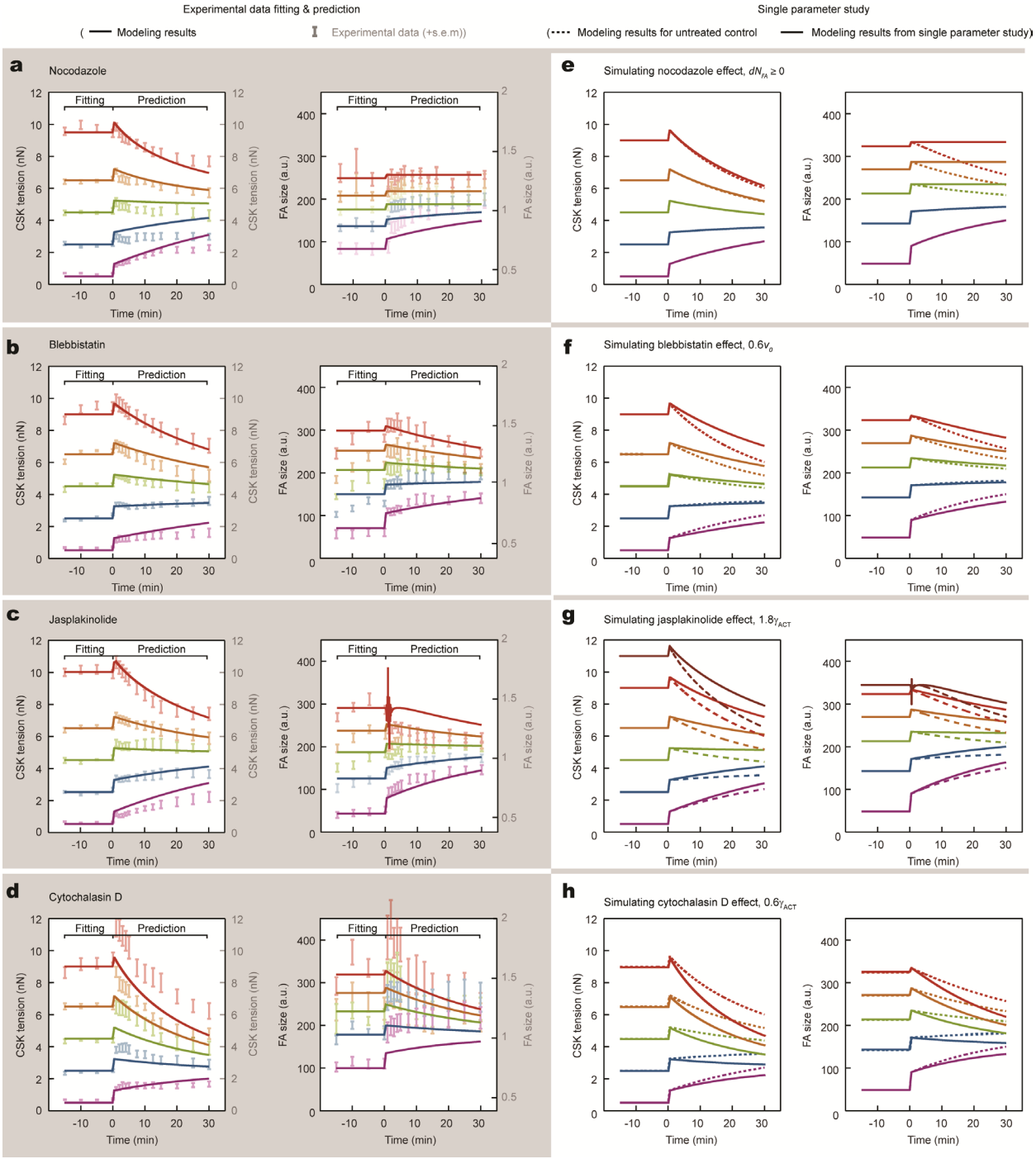

Supplementary Figure 15. Recapitulation and prediction of mechanosensitive rheostasis of subcellular cytoskeleton (CSK) tension and focal adhesion (FA) for REF-52 fibroblasts under 8% static equibiaxial stretch and treated with small-molecule inhibitors as indicated. (**a-d**)

Theoretical calculations of rheostatic responses of CSK tension (*left*) and FA size (*right*) plotted against time (solid curves), agreeing reasonably well with experimental data (translucent error bars). Ground-state values of CSK tension and FA size obtained for $t \leq 0$ min were used for calculations of best-fit model parameters, which were then employed for calculations of rheostatic paths for $t > 0$. (**e-h**) Single-parameter studies to theoretically elucidate the role of individual CSK components in subcellular rheostasis. Theoretical calculations of rheostatic responses of CSK tension (*left*) and FA size (*right*) were conducted using modified model parameters as indicated (solid curves). Modeling results for untreated control (dashed curves) were plotted together for comparison. In **e**, temporal change of FA size dN_{FA}/dt was set ≥ 0, to simulate the effect of nocodazole treatment on preventing FA disassembly. There was no significant change in rheostatic behavior of CSK tension. However, relaxation of FA rheostasis in *Phase II* was inhibited. In **f**, the equivalent sliding velocity of myosin motor v_o was decreased from the value for untreated control to simulate the effect of blebbistatin treatment on reducing myosin II activity, resulting in slower rheostatic responses in *Phase II* for both CSK tension and FA. In **g**, to mimic the effect of jasplakinolide, the dimensionless association rate of actin subunits γ_{ACT} was increased from the value for untreated control. The abolished initial FA strengthening in *Phase I* for FA subsets sustaining high CSK tension was due to instability of theoretical modeling (see discussions in **Biophysical modeling** and **Supplementary Figure 16d**). In **h**, the dimensionless association rate of actin subunits γ_{ACT} was decreased from the value for untreated control, to mimic reduced association of actin monomers onto the barbed end of actin filaments due to cytochalasin D treatment. This modification of model parameter resulted in faster relaxation yet slower reinforcement for both CSK tension and FA in *Phase II*.

Supplementary Figure 16

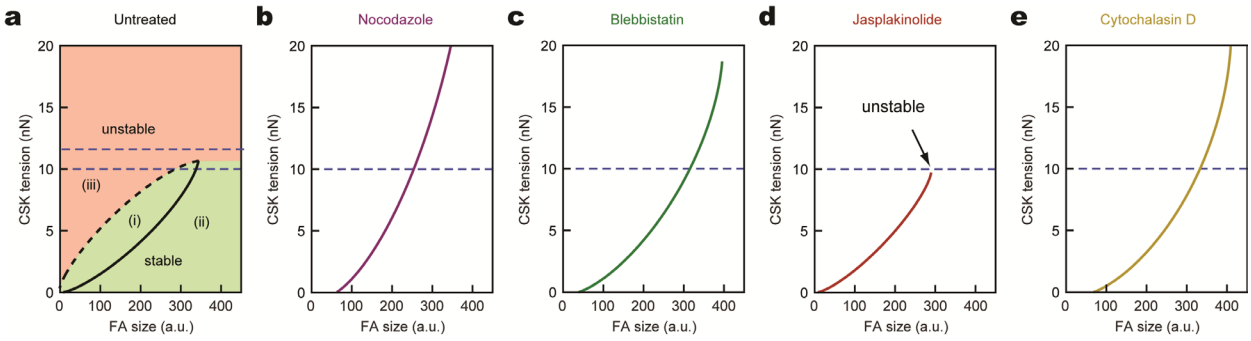

Supplementary Figure 16. Stability of focal adhesions (FAs) under cytoskeleton (CSK) tension. Steady-state solutions calculated from Equ. (4) were plotted, showing positive correlations between FA size and CSK tension (see discussions in **Biophysical modeling**). Briefly, the ordinary differential equation governing force-dependent dynamic evolution of FA size N_{FA} (Equ. (4)) had two steady-state solutions (Equ. (9): dashed black curve; Equ. (10): solid black curve), dividing the two-dimensional space with N_{FA} and F_{tot} as the *x*- and *y*-axes, respectively, into three regions, as illustrated in **a**. The steady-state solution corresponding to Equ. (10) was stable, since all transient states falling into *region i* and *region ii* would be driven by governing equations to approach it, suggesting that small fluctuations from the solid black curve would quickly regress with CSK tension and FA restoring their stable equilibrium states in a quasi-static manner. The steady-state solution corresponding to Equ. (9) was at the boundary between unstable and stable regimes, and any fluctuation from this boundary could either regress to the stable steady-state curve or become divergent and unstable. With mild external stimulations, the CSK-FA system was able to adjust around the stable steady-state curve (solid black curve) and restore their stable equilibrium states. Therefore, stability of the CSK-FA system was limited by the end-point of the stable steady-state curve, beyond which steady-state solutions became unavailable and both FA and actin stress fiber would undergo rapid

disassembly. For example, FA bearing CSK tension force of 12 nN that exceeded the limit for untreated cells would become unstable (**a**). Steady-state solution curves calculated from Equ. (10) were also dependent on the integrity of the CSK (**b-e**). Thus, small-molecule inhibitor treatments targeting CSK components could change stable steady-state solution curves as well as stability of FA under CSK tension. For example, FA bearing 10 nN CSK tension was stable in untreated cells (**a**); however, it became unstable in jasplakinolide-treated cells (**d**).

Supplementary Figure 17

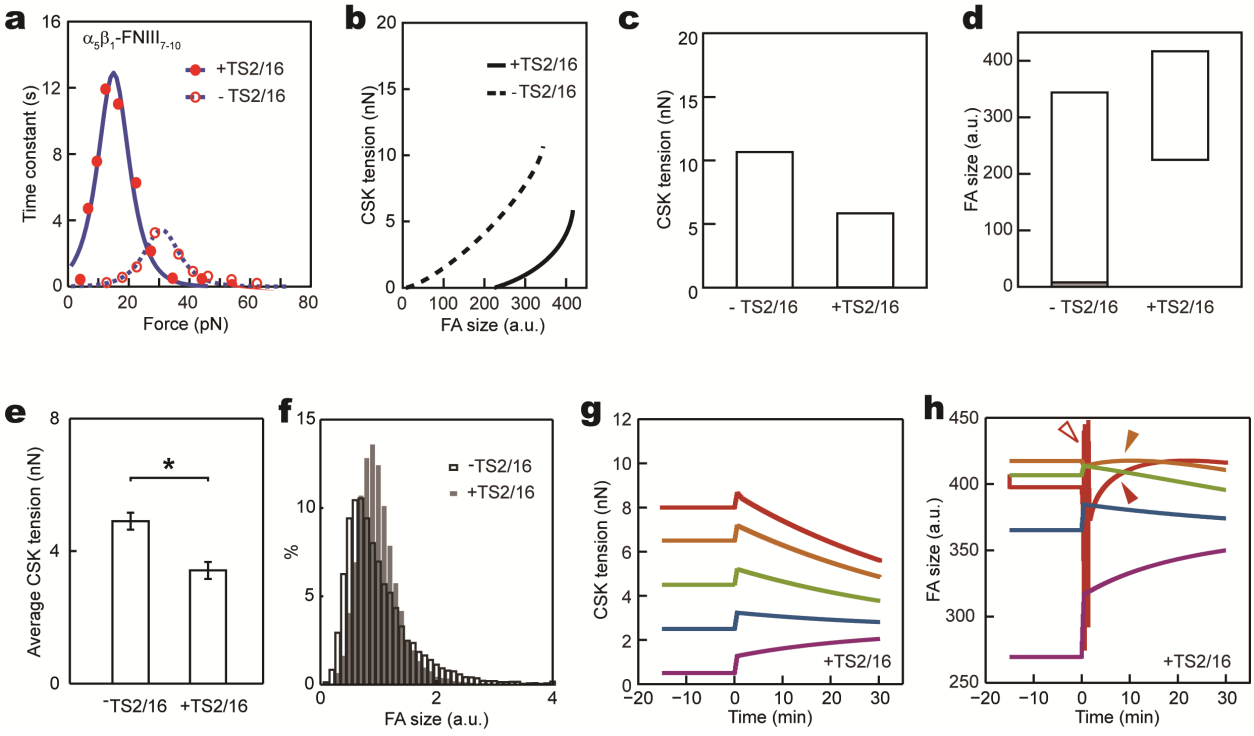

Supplementary Figure 17. Significance of integrin catch-slip bond in regulating mechanosensitive rheostasis of subcellular cytoskeleton (CSK) tension and focal adhesion (FA). (**a**) Force - lifetime diagram of the catch-slip bond between $\alpha_5\beta_1$ integrin and $FNIII_{7\text{-}10}$, with or without treatments of integrin $\beta1$ antibody TS2/16 as indicated (data from Ref. [11]). Treatment of TS2/16 significantly changes catch-slip bond dynamics by shortening bond lifetime under high forces and prolonging bond lifetime at low forces. To determine catch-slip bond parameters, the two-pathway model (solid blue curve; Equ. (3)) was used for fitting experimental data (red dots) from Kong *et al.*[1] for TS2/16-treated cells, with best-fit parameters $\phi_{FA,s} = 7.65$, $\phi_{FA,c} = 0$, and $f_{FA}^{*} = 4.6$ pN. Experimental data for untreated control as well as its associated best fitting curve generated from the two-pathway model (red open circles and dashed blue curve) were plotted for comparison. (**b**) Stable steady-state solutions of CSK tension *vs.* FA size, with or without treatments of TS2/16 as indicated. Treatment with TS2/16 modified correlations

between FA size and CSK tension, and it further stabilized FA under low force but reduced the maximum CSK tension sustained by FA under steady-state conditions. (**c&d**) Theoretical predictions of changes in CSK tension (**c**) and FA size (**d**) upon TS2/16 treatment. Data was extracted from **b**. (**e&f**) Experimental results showing reduction of CSK tension (**e**) and a shift of FA size distribution toward large FAs (**f**) upon TS2/16 treatments for human mesenchymal stem cells (HUMSCs). (**g&h**) Theoretical calculations of rheostatic behaviors of CSK tension (**g**) and FA size (**h**) for TS2/16-treated cells. Best-fit parameters $\phi_{FA,s}$, $\phi_{FA,c}$, and f_{FA}^{*} obtained from **a** for TS2/16-treated cells were used for calculation, together with other model parameters determined by fitting ground-state values of CSK tension and FA size in REF-52 fibroblasts. Hollow red arrowhead indicated instability of FA response in *Phase I*, whereas solid red and orange arrowheads marked reinforcement of FA in *Phase II*.

Supplementary Figure 18

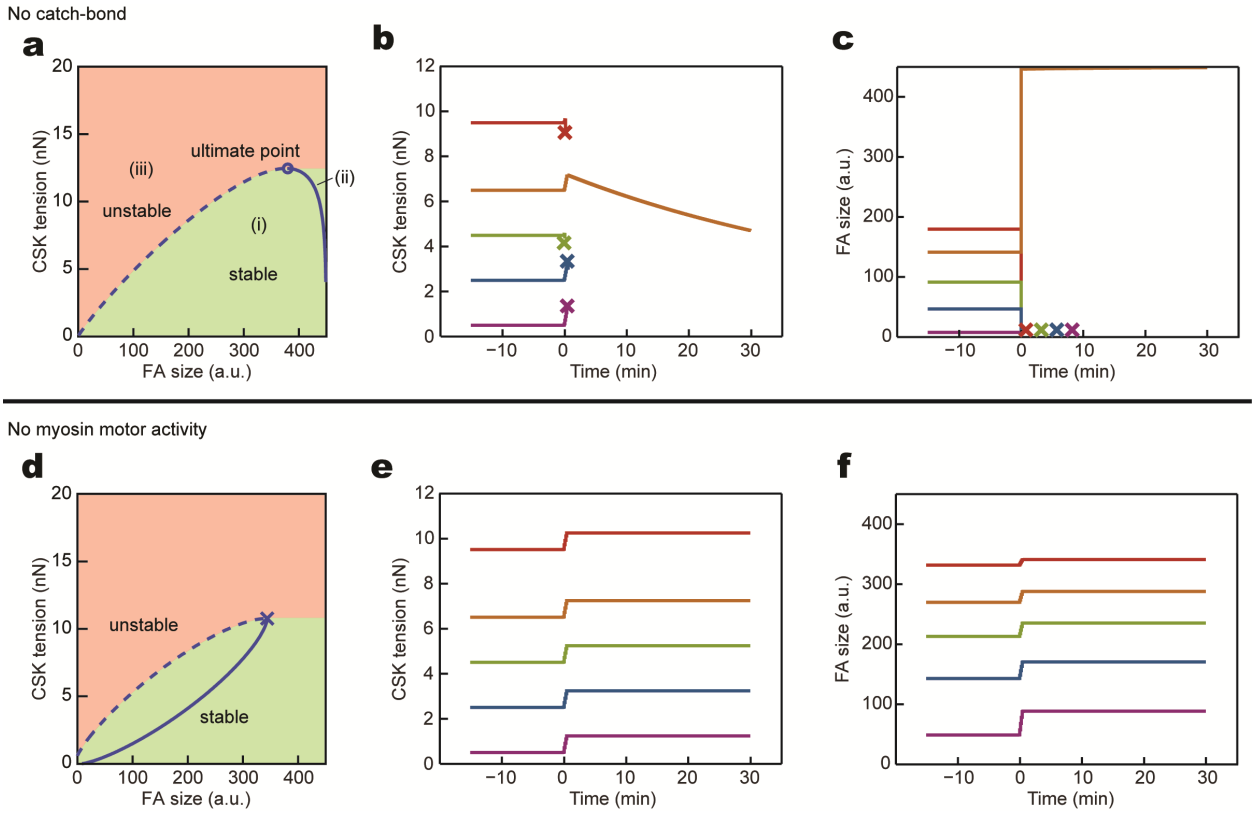

Supplementary Figure 18. Indispensability of catch-slip bond and myosin motor activity in mediating mechanosensitive rheostasis of subcellular cytoskeleton (CSK) tension and focal adhesion (FA). Dynamic responses of CSK tension and FA to static cell stretch were simulated using a modified biophysical model without the catch-bond portion of the integrin catch-slip bond (**a-c**) or myosin motor activity (**d-f**) (see discussions in **Biophysical modeling**). (**a-c**) Stable steady-state solution of CSK tension *vs.* FA (solid blue curve) obtained from the modified model without the catch-bond portion of the integrin catch-slip bond would suggest ground-state values of FA unrealistically large and independent of CSK tension. Small perturbations to the CSK-FA system on the unstable portion of the steady-state curve (dashed blue curve) would result in FAs to either be completely dissolved or grow to its maximum size when perturbed to fall into *region iii* or *region i*, respectively. Such hypersensitivity of the CSK-FA system without

catch bonds would also lead to spontaneous disassembly of majority of FAs upon cell stretch (**b&c**). FAs surviving from the initial phase would grow to its maximum size regardless of CSK tension (**c**), contradictory to experimental observations of subcellular rheostasis of CSK tension and FA. (**d-f**) Theoretical modeling without considering myosin motor activity. Steady-state solution of CSK tension *vs.* FA obtained from the modified model was not affected by the removal of myosin motor activity in theoretical modeling. However, upon cell stretch, both CSK tension (**e**) and FA size (**f**) could only demonstrate reinforcement in *Phase I*, but not exhibiting rheostatic behaviors (reinforcement or relaxation) during *Phase II*.

SUPPLEMENTARY TABLE

Sym.	Definition	*U*	*N*	*B*	*J*	*C*	*T*
N_{FA}	FA size	OUT	-	-	-	-	-
$k_{FA,o}$	Reference rate for FA association and dissociation (s^{-1})	1	-	-	-	-	-
N_{FA}^{tot}	Total number of FA unit available in the cytosol	450	-	-	-	-	-
γ_{FA}	Non-dimensional association rate for FA	1	-	-	-	-	-
f_{FA}^{*}	Force scale for non-dimensionalization (pN)	5.38[1]	18.83	9.68	6.46	10.76	4.60[1]
$\phi_{FA,s}$	See Equ. (3)	7.78[1]	-	-	6.61	-	7.65[1]
$\phi_{FA,c}$	See Equ. (3)	4.02[1]	1.81	2.41	-	1.73	0[1]
N_{ACT}	Actin subunits in stress fiber	OUT	-	-	-	-	-
$k_{ACT,o}$	Reference rate for actin association and dissociation	1	-	-	-	-	-
N_{ACT}^{tot}	Total number of actin subunit available in the cytosol	9000	-	-	-	-	-
γ_{ACT}	Non-dimensional association rate for actin	1	2	-	1.8	0.6	-
f_{ACT}^{*}	Force scale for non-dimensionalization (pN)	10.68[2]	-	-	-	-	-
$\phi_{ACT,s}$	See Equ. (4)	2.42[2]	-	-	-	-	-
$\phi_{ACT,c}$	See Equ. (4)	1.43[2]	-	-	-	-	-
F_{tot}	Total force on FA cluster and actin stress fiber	OUT	-	-	-	-	-
K_{post}	Spring constant of micropost (pN/μm)	7200[17]	-	-	-	-	-
K_{SF}	Spring constant of actin stress fiber (pN/μm)	157[13-14]	-	-	-	-	-
L	Length of spring-CE system; stretch profile	INP	-	-	-	-	-
v_o	Equivalent unloaded sliding velocity of myosin (μm/s)	0.012[16]	0.015	0.0072	-	-	-
f_{stall}	Stall force of myosin (pN)	2[15]	-	-	-	-	-
c	Ratio of myosin number to actin subunit number	0.469	-	-	-	-	-

Supplementary Table 1. *U*: untreated; *N*: nocodazole treatment; *B*: blebbistatin treatment; *J*: jasplakinolide treatment; *C*: cytochalasin D treatment; *T*: TS2/16 antibody treatment; INP:

input of the model; OUT: output of the model; -: same as untreated control. If references were not listed, then model parameters were determined by fitting ground-state values of cytoskeleton (CSK) tension and focal adhesion (FA) size for REF-52 fibroblasts under conditions as specified.

SUPPLEMENTARY REFERENCES

1 Kong, F., García, A. J., Mould, A. P., Humphries, M. J. & Zhu, C. Demonstration of catch bonds between an integrin and its ligand. *J. Cell Biol.* **185**, 1275-1284 (2009).

2 Lee, C.-Y. *et al.* Actin depolymerization under force is governed by lysine 113:glutamic acid 195-mediated catch-slip bonds. *Proc. Natl. Acad. Sci. USA* **110**, 5022-5027 (2013).

3 Mitrossilis, D. *et al.* Single-cell response to stiffness exhibits muscle-like behavior. *Proc. Natl. Acad. Sci. USA* **106**, 18243-18248 (2009).

4 Novikova, Elizaveta A. & Storm, C. Contractile fibers and catch-bond clusters: A biological force sensor? *Biophy. J.* **105**, 1336-1345 (2013).

5 Pereverzev, Y. V., Prezhdo, O. V., Forero, M., Sokurenko, E. V. & Thomas, W. E. The two-pathway model for the catch-slip transition in biological adhesion. *Biophy. J.* **89**, 1446-1454 (2005).

6 del Rio, A. *et al.* Stretching single talin rod molecules activates vinculin binding. *Science* **323**, 638-641 (2009).

7 Hirata, H., Tatsumi, H., Lim, C. T. & Sokabe, M. Force-dependent vinculin binding to talin in live cells: A crucial step in anchoring the actin cytoskeleton to focal adhesions. *Am. J. Physiological.-Cell Physiol.* **306**, C607-C620 (2014).

8 Rognoni, L., Stigler, J., Pelz, B., Ylänne, J. & Rief, M. Dynamic force sensing of filamin revealed in single-molecule experiments. *Proc. Natl. Acad. Sci. USA* **109**, 19679-19684 (2012).

9 Ferrer, J. M. *et al.* Measuring molecular rupture forces between single actin filaments and actin-binding proteins. *Proc. Natl. Acad. Sci. USA* **105**, 9221-9226 (2008).

10 Parmley, W. W. & Sonnenblick, E. H. Series elasticity in heart muscle. Its relation to contractile element velocity and proposed muscle models. *Circ. Res.* **20**, 112-123 (1967).

11 MacIntosh, B. R. & MacNaughton, M. B. The length dependence of muscle active force: Considerations for parallel elastic properties. *J. Appl. Physiol.* **98**, 1666-1673 (2005).

12 Hill, A. V. The heat of shortening and the dynamic constants of muscle. *P. Roy. Soc. Lond. B. Bio.* **126**, 136-195 (1938).

13 Kumar, S. *et al.* Viscoelastic retraction of single living stress fibers and its impact on cell shape, cytoskeletal organization, and extracellular matrix mechanics. *Biophys. J.* **90**, 3762-3773 (2006).

14 Lu, L., Oswald, S. J., Ngu, H. & Yin, F. C. P. Mechanical properties of actin stress fibers in living cells. *Biophys. J.* **95**, 6060-6071 (2008).

15 Veigel, C., Molloy, J. E., Schmitz, S. & Kendrick-Jones, J. Load-dependent kinetics of force production by smooth muscle myosin measured with optical tweezers. *Nat. Cell Biol.* **5**, 980-986 (2003).

16 Finer, J. T., Simmons, R. M. & Spudich, J. A. Single myosin molecule mechanics: Piconewton forces and nanometre steps. *Nature* **368**, 113-119 (1994).

17 Fu, J. *et al.* Mechanical regulation of cell function using geometrically modulated elastomeric substrates. *Nat. Methods* **7**, 733-736 (2010).